Nano Energy 111 (2023) 108427

Contents lists available at ScienceDirect

Nano Energy

journal homepage: www.elsevier.com/locate/nanoen

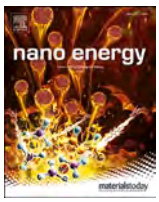

Revealing the conductivity stability of 2D Cu-MOFs as flexible electrodes: demonstration of triboelectric nanogenerators

Yinghong Wu [a,*], Yang Luo [b,*], Paul K. Chu [b], Carlo Menon [a,*]

[a] Biomedical and Mobile Health Technology Lab, Department of Health Sciences and Technology, ETH Zürich, Lengghalde 5, Zürich, 8008, Switzerland
[b] Department of Physics, City University of Hong Kong, Tat Chee Avenue, Kowloon, Hong Kong, 999077, China

ARTICLE INFO

Keywords:
Conductive metal-organic frameworks
Flexible electrode
Conductivity stability
Triboelectric nanogenerator
Energy harvesting

ABSTRACT

Owing to the high electron delocalization in 2D ultrathin regions derived from π-d conjugations, electrically conductive metal-organic frameworks (MOFs) are widely used in electronic applications but mostly for rigid devices. The interaction mechanism between conductive 2D MOFs and flexible substrates remains unclear, which cannot meet the increasing demand for next-generation wearable electronics. Herein, conductive copper-benzenehexathiol (Cu-BHT) layers are developed and the underlying mechanisms responsible for the conductivity difference on different representative substrates are explored. It is found that not only the molecular movement inside the polymer but also the fusion between polymer and Cu-MOFs affects the intrinsic conductivity and long-term stability. Therefore, the potential guiding criteria for selecting flexible substrates for conductive 2D MOFs are established. As a demonstration, the Cu-BHT/polymer layer is considered the flexible electrode of triboelectric nanogenerators to harvest energy from water droplets and human motions, verifying the significant role of conductive 2D MOFs in flexible and wearable applications. This study reveals the insights to the potential interaction effect on the conductivity stability of Cu-BHT and advances the development of 2D conductive MOFs in flexible and wearable electronics.

1. Introduction

Metal-organic frameworks (MOFs), consisting of organic ligands and metal nodes/clusters, are an emerging class of crystalline coordination polymers. Owing to advantages such as component tunability, inherent porosity, as well as tailorable surface properties, MOFs have attracted increasing attention in a myriad of areas including catalysis [1], biomedicine [2], sensors [3], as well as energy storage and conversion [4]. In recent years, explorations of MOFs have been extended to the energy harvesting field, in which triboelectric nanogenerator (TENG), based on contact electrification and electrostatic induction, is considered one of the most promising energy harvesters, owing to its merits of compact structure, simple fabrication, broad material selection, as well as high conversion efficiency [5–8].

Typically, MOFs are often employed as triboelectric materials of TENGs owing to their tunable functional frameworks and designable morphologies. For example, Khandelwal et al. [5] reported one of the most popular MOFs, zeolitic imidazole framework-8 (ZIF-8), as a novel triboelectric material for self-powered sensors and systems. They then investigated other ZIF subfamily materials such as ZIF-7 and ZIF-62 to explore potential applications of MOFs-TENGs in electronics powering and energy harvesting in sports [9,10]. Meanwhile, Mi's group utilized MOFs as friction power generation materials and claimed that a higher conjugation degree could reduce the band gap and thus enhance the output of MOFs-TENG [8]. Instead of treating MOFs as triboelectric positive materials, Guo et al. [6] incorporated a fluorinated MOF into PDMS to improve the negative triboelectricity of MOFs-TENG. Because of increased charges, surface roughness, and capacitance after introducing fluorinated MOF, the developed TENG showed a significant output increase. Similar designs by considering either bare MOFs or MOFs composites as triboelectric materials have also been reported in other works [11–13]. However, up to date, the applications of conventional MOFs in the field of TENGs are far from expectations; for example, they still cannot be used as electrode materials for TENGs mainly because of the poor or no electrical conductivity.

In 2015, a novel two-dimensional (2D) MOF, copper-benzenehexathiol (Cu-BHT), was reported to have an extremely high conductivity of 750–1580 S/cm by taking advantages of strong π-d conjugation and electron delocalization in the 2D lattice [14]. Since then, several theoretical and experimental studies have further

* Corresponding authors.
E-mail addresses: yinghong.wu@hest.ethz.ch (Y. Wu), yluo24-c@my.cityu.edu.hk (Y. Luo), carlo.menon@hest.ethz.ch (C. Menon).

https://doi.org/10.1016/j.nanoen.2023.108427
Received 5 January 2023; Received in revised form 3 April 2023; Accepted 5 April 2023
Available online 6 April 2023

demonstrated the good electrical conductivity (10^2-10^3 S/cm) of Cu-BHT [15–18]. Meanwhile, the applied roles of Cu-BHT MOFs have also been explored in areas such as hydrogen evolution catalysis [19], photovoltaic solar cells [20], lithium-ion batteries [21], as well as sensing [22,23]. We believe the emergence of this kind of novel materials opens opportunities to develop promising conductive MOFs-based electrodes for TENGs. However, to the best of our knowledge, neither Cu-BHT nor other conductive MOFs has been reported as electrodes in TENGs. More importantly, up to date, Cu-BHT was mainly used for rigid devices in most previous studies, which is far from enough for flexible and wearable electronics with rapid development and increasing popularity in daily life. Although a few works mentioned the potential of Cu-BHT on flexible substrates [20,24], no reports have ever investigated how flexible substrates may affect the conductivity and long-term stability of Cu-BHT. However, those are crucial factors influencing the understanding and development of Cu-BHT and other conductive 2D MOFs in future flexible and wearable applications.

Herein, conductive and ultrathin Cu-BHT films are synthesized by a self-assembly coordination reaction at the liquid-liquid interface. To evaluate the stability-affecting mechanisms of Cu-BHT in flexible occasions, representative polymers with different material properties are selected as flexible substrates. Interestingly, the obtained Cu-BHT layers on various substrates show huge differences in both initial and long-term conductivity. To determine why and how these flexible substrates affect the conductivity stability of Cu-BHT, the intrinsic properties of polymers and the interaction mechanism between Cu-BHT and polymers are investigated. It is found that, the internal molecular movement of the substrates and the fusion between polymer and Cu-BHT at the interface are mainly responsible for the conductivity difference. To further assess the practical potential in flexible and wearable devices, the Cu-BHT/polymer layer is employed as an electrode of TENG. The flexible Cu-BHT-based TENG can efficiently harvest not only droplet energy from different types of water, but also human motion energy for electronics powering. The developed strategies and knowledge provide guidance pertaining to the development of 2D MOFs electrodes for high-performance flexible and wearable devices.

2. Results and discussion

Fig. 1a schematically illustrates the self-assembly of Cu-BHT based on a coordination reaction between Cu^{2+} and the ligand of BHT. In this work, spin-coating is performed to form Cu-BHT films on target substrates. After the Cu^{2+} and BHT solutions are spread on the plasma-treated substrates (Fig. S1), the coordination reaction proceeds at the interface immediately as illustrated in Fig. 1a,b. The BHT molecules deprotonate first and then act as ligands to coordinate with the Cu cation centers to form a solid two-dimensional supramolecular structure during the self-assembly. The π-d conjugation ensures the stability of this 2D structure. With the removal of excess solutions, a uniform and full-coverage Cu-BHT layer with transparency of >80 % in the visible light

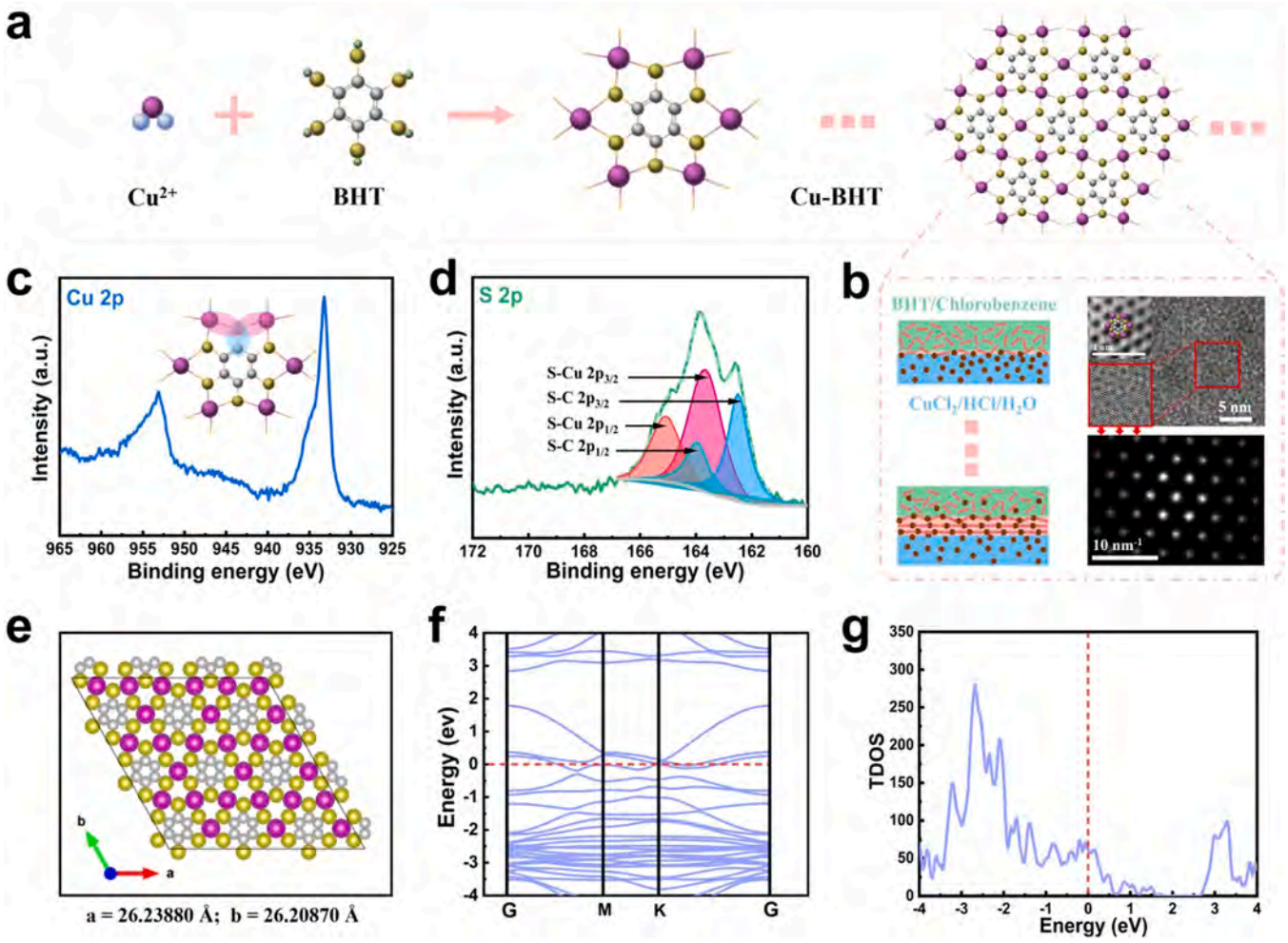

Fig. 1. Synthesis and conductivity prediction of Cu-BHT: a Schematic diagram of coordination reaction and synthesis of Cu-BHT, **b** schematic diagram of synthesis process of Cu-BHT and AC-HAADF-STEM and FFT images, **c,d** high-resolution XPS spectra of Cu *2p* and S *2p* of Cu-BHT, **e** theoretical Cu-BHT model for DFT the calculation, **f** calculated band structures, and **g** total density of states for Cu-BHT structure.

range is obtained as shown in Fig. S2. The transmission electron microscopy (TEM) and high-resolution TEM (HR-TEM) images in Fig. S3 confirm the ultrathin 2D morphology of the synthesized Cu-BHT film. The corresponding hexagonal fast Fourier transform (FFT) pattern and the atomic image acquired by spherical-aberration-corrected high-angle annular dark-field scanning transmission electron microscopy (AC-HAADF-STEM) in Fig. 1b provide evidence of the highly crystalline and intact hexagonal atomic arrangement of Cu-BHT (distance between neighboring benzene rings measured to be ~8.5 Å) within a kagome network. The π-d conjugation kagome network and π-π stacking between 2D lattices endow the Cu-BHT films with very promising conductivity within the MOFs family.

Moreover, the XRD pattern in Fig. S4 is consistent with reported Cu-BHT [17,21,22], confirming the successful synthesis. The Raman scattering spectroscope (Raman) and the attenuated total reflection (ATR) infrared spectroscope were used to reveal the evolution of chemical bonds during the coordination reaction. As shown in Fig. S5, the S–H peak (2501.1 cm^{-1}), C═C peak (1477.3 cm^{-1}) and overlapped C–C and C–S bonds (1136.3 cm^{-1}) are sourced from BHT. It is noted that the existence of S–S peak (460.2 cm^{-1}) is due to the inevitably slight oxidation of BHT to sulfur with the long-term storage, which shows negligible impact on the coordination reaction between the metal ion Cu^{2+} and the ligand BHT. With the formation of Cu-BHT, the S–H bonds disappear completely and the S–Cu peak (342.3 cm^{-1}) and benzene ring deformation (broad peak at ~350–500 cm^{-1}) appear, verifying full coordination of Cu (I) with S–H to produce the well-organized Cu-BHT network. The consistency of Raman and ATR-IR results confirms the accuracy and reproducibility of the measurements.

The survey X-ray photoelectron spectroscopy (XPS) spectrum in Fig. S6 shows the presence of copper, sulfur, carbon, as well as a small amount of oxygen from air exposure. The high-resolution Cu *2p* region in Fig. 1c consists of two spin-orbit peaks corresponding to Cu $2p_{3/2}$ and Cu

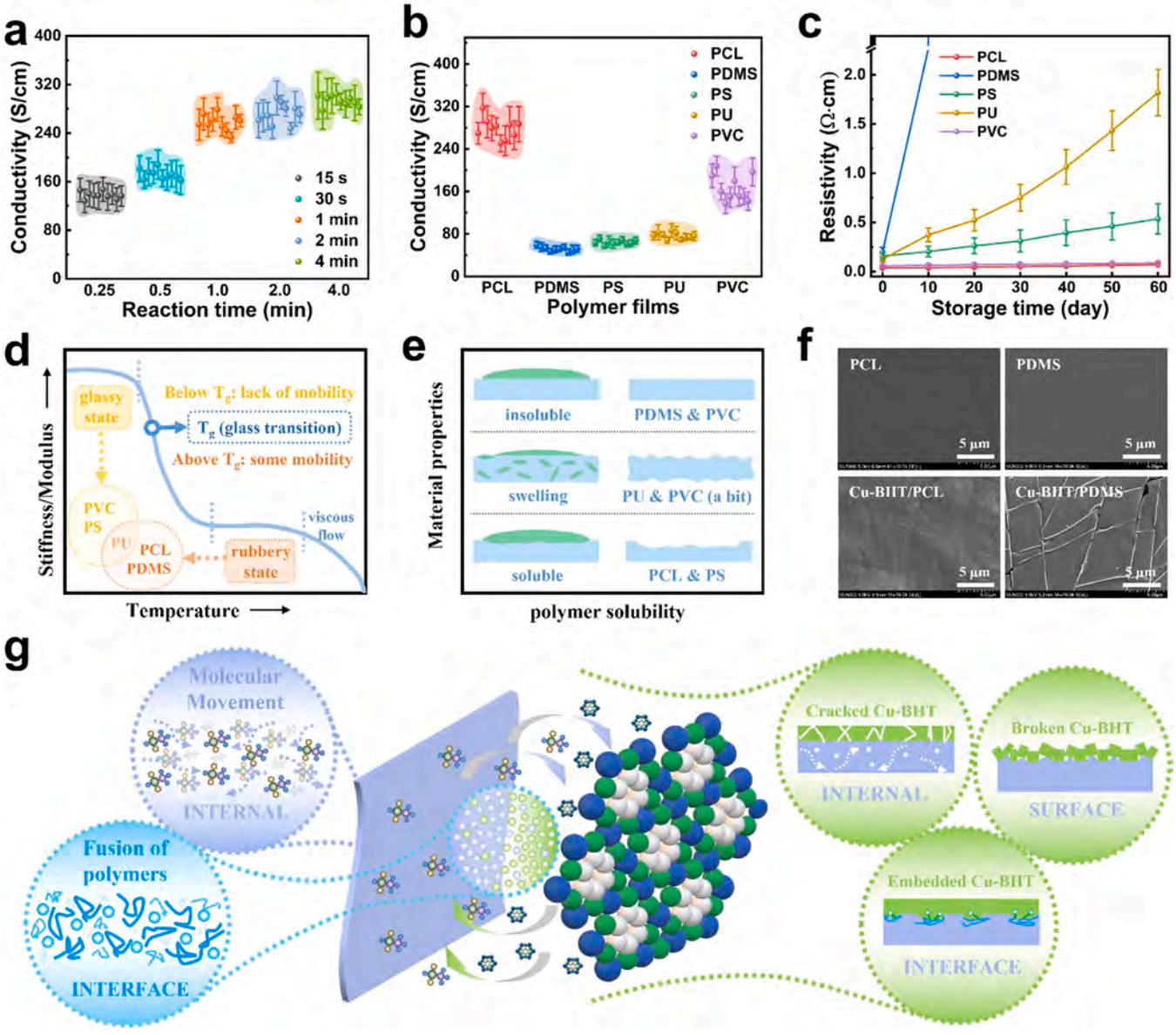

Fig. 2. Underlying reasons contributing to the conductivity difference of Cu-BHT on different polymer substrates: a effect of the reaction time on the conductivity of Cu-BHT, **b** effect of the polymer substrates on the conductivity of Cu-BHT, **c** resistivity stability of the Cu-BHT/polymer films during two-month storage, **d** glassy or rubbery states of various polymer substrates, **e** chlorobenzene solvent solubility of various polymer substrates, and **f** SEM images of PCL and PDMS films with or without Cu-BHT, and **g** mechanism schematic diagrams of main factors affecting the initial and long-term conductivity of Cu-BHT on different polymer substrates.

$2p_{1/2}$ of Cu (I) at 933.1 eV and 953.1 eV, respectively. The Cu (II) satellite peak cannot be observed implying that Cu (II) is completely reduced to Cu (I) in the reaction. In the π-d conjugated Cu-BHT, the S *2p* orbitals are bonded with both Cu *d* orbitals and C *π* orbitals. As shown in the S *2p* spectrum (Fig. 1d), the merged doublets are composed of the $2p_{3/2}$ spin-orbital and $2p_{1/2}$ spin-orbital of S–Cu bonds and S–C bonds. By means of Gaussian deconvolution, four convoluted peaks can be identified at 162.4, 163.6, 163.8 and 165.0 eV representing S–C $2p_{3/2}$, S–Cu $2p_{3/2}$, S–C $2p_{1/2}$, and S–Cu $2p_{1/2}$, respectively. The peak area of S–Cu is approximately twice that of S–C, depicting the coordination structure shown in the inset of Fig. 1c. This verifies the successful formation of full *π-d* conjugation in $[Cu_3(C_6S_6)]_n$ 2D lattice, which is the origin of the metallic feature [18,25]. In this case, the theoretical and experimental conductivity of Cu-BHT is further investigated.

The theoretical Cu-BHT model used in the density functional theory (DFT) calculation is exhibited in Fig. 1e. The perfect Cu-BHT primitive cell is constructed with in-plane lattice constants of a = 26.24 Å and b = 26.21 Å according to previous theoretical and experimental results [14,22,26]. The derived band structure (Fig. 1f) and total density of states (TDOS, Fig. 1g) indicate that Cu-BHT should theoretically exhibit overlapping band waves at the Fermi level with intrinsic high conductivity and metallic features. This results from strong *π-d* conjugation in 2D lattices and *π-π* stacking between the 2D layers providing a large free electron concentration and high electron mobility [27,28].

Normally, the practically measured conductivity (in the semimetallic range) is lower than the theoretically predicted values due to the electron transport hindering from the existing grain boundaries in polycrystalline Cu-BHT films [29,30]. As shown in Fig. 2a, as the reaction time is increased from 15 s to 4 min, the conductivity of the formed Cu-BHT films increases first and then stabilizes. It is noted that the reaction time between BHT ligand and Cu ions enables to control the thickness of the formed Cu-BHT film. The increased reaction time shows a positive effect on the conductivity of the Cu-BHT film. This is mainly because of the increased thickness and crystallinity but decreased grain boundaries of the formed Cu-BHT films, which can be confirmed by the atomic force microscopy (AFM) images in Fig. S7. With increasing the reaction time from 15 s to 1 min, the thickness of the formed Cu-BHT film increases from ~6.5 nm to ~10.1 nm and the grain boundaries gradually become blurred. With the reaction time further increased to 2 min and 4 min, no obvious change in film thickness is observed and the grain boundaries disappear. Consequently, a reasonable phenomenon is observed from the transmittance of these samples, where high transparency of > 90 % is observed (Fig. S9a) when the reaction time is only 15 s but decreases to > 80 % when the reaction time is longer than 1 min. Hence, the coordination reaction is completed at around 1 min with the full consumption of the BHT component, and the reaction time of the following samples in this work is all set at 1 min

Most previous works have verified the high experimental conductivity of Cu-BHT on rigid substrates such as glass and silicon wafer [14,20,23]. However, there have been very few studies on the use of Cu-BHT on flexible substrates, which limits its practical applications in flexible and wearable electronics. Herein, representative polymer films including PCL [polycaprolactone], PDMS [polydimethylsiloxane], PS [polystyrene], PU [polyurethane], and PVC [polyvinyl chloride]) are chosen as flexible substrates to reveal the interaction between Cu-BHT and polymer at the interface. Fig. S9b shows that the Cu-BHT films prepared on different polymers have similar transmittance (70–85 %). Interestingly, the conductivity of Cu-BHT film on these polymer substrates, however, is totally different as seen in Fig. 2b. For example, the Cu-BHT/PCL and Cu-BHT/PVC films exhibit a higher conductivity of 250–300 S/cm and 150–200 S/cm, respectively, while the Cu-BHT/PDMS films have a lower conductivity of 40–60 S/cm. The conductivity of the other two films is also different from each other, showing a decreasing order of PCL > PVC > PU > PS > PDMS under the same synthesis and measurement conditions.

More intriguingly, the conductivity stability of the different Cu-BHT/polymer films showed even larger differences during two-month storage under ambient conditions. As shown in Fig. 2c, both the Cu-BHT/PCL and Cu-BHT/PVC films exhibit stable resistivity during storage, but the resistivity of the other three Cu-BHT/polymer (PS, PU, PDMS) films shows an obviously increasing tendency. In particular, the resistivity of Cu-BHT/PDMS increases from ~0.2 Ω·cm to more than 10 Ω·cm in ten days, boding ill for electronic applications. Therefore, it is of great importance to determine the underlying reasons for the initial conductivity and long-term stability differences of Cu-BHT when forming on different polymer substrates. Since the coordination reaction always occurs at the liquid-liquid interface among Cu^{2+} and BHT solutions, substrates with different physical and chemical properties should not affect the synthesis of Cu-BHT. Therefore, the short and long-term conductivity differences of Cu-BHT on the different polymer substrates should be attributed to underlying mechanisms after the formation of Cu-BHT.

First and foremost, the glassy or rubbery states of polymer substrates may affect both the initial and long-term conductivity of Cu-BHT layers. As shown in Fig. 2d, as the temperature is raised, the materials change from a relatively hard/brittle glassy state to a relatively soft/flexible rubbery state. The glass transition temperature (T_g) of various materials is quite different depending on the material properties. Usually, if the environmental temperature is higher than the T_g of a material, there is some mobility on the molecular level. As shown in Fig. S10a, both PS and PVC have a T_g higher than 80 °C and are considered as hard plastics in the glassy state. However, PCL, PDMS and PU are soft plastics/elastomers in the rubbery state as their T_g is below zero. Ideally, Cu-BHT, as a relatively hard polymer, should "prefer" the glassy materials better than the rubbery/elastic materials during spin coating. More importantly, the internal molecular mobility of the soft polymers may lead to the instability of the covered Cu-BHT. This could explain why the Cu-BHT/PVC film still has great conductivity after storage but Cu-BHT/PDMS film shows the worst initial and long-term conductivity. Compared to the ignorable surface change of PVC before and after Cu/BHT formation in Fig. S11, the Cu-BHT layer on the PDMS surface shows cracks (Fig. 2f), even though the original PDMS surface is quite smooth. It is potentially because the molecular movement inside PDMS induces the formation of cracked Cu-BHT. Comprising both glassy and rubbery chains, PU is considered as a middle-of-the-road material. Hence, its short and long-term stability in conductivity falls between that of hard materials (PVC) and soft elastomers (PDMS). However, this theory is not enough to explain the Cu-BHT conductivity performance on PCL that is also a soft plastic, and other factors causing this phenomenon need to be explored.

The second mechanism could be the fusion of Cu-BHT and polymer substrates. After spin-coating, a small amount of the solvent commonly remains on the substrate until it evaporates. None of the five polymer substrates (PCL, PDMS, PS, PU, PVC) dissolve in water ($CuCl_2$/HCl/H_2O here), but they respond differently to the BHT/chlorobenzene solution as schematic in Fig. 2e. When BHT/chlorobenzene droplets are placed on the PDMS substrate, there is almost no change on the surface until the solvent evaporates totally (Fig. S10b). Similar but with a bit swelling phenomenon can be observed on the PVC substrate and it almost returns to the original state after solvent evaporation. Therefore, the solvent can barely affect the PVC substrate as well. However, obvious swelling occurs at first and then a shrinking and uneven surface is observed from the PU substrate. Thus, it is no doubt that lots of small pieces of Cu-BHT layers emerge on the PU substrate in Fig. S11, which is another factor contributing to its lower conductivity. While for PS and PCL, they can be absolutely dissolved by chlorobenzene, which may lead to the fusion of Cu-BHT and PCL/PS at the interface. Therefore, embedded Cu-BHT layers are stably formed on both PCL (Fig. 2f) and PS surfaces (Fig. S11), which is further verified by the insignificant conductivity change before and after water rinse (Fig. S10c). Consequently, the Cu-BHT/PCL film performs not only excellent initial conductivity but also long-term stability. However, the Cu-BHT/PS film does not show the

same or similar performance, which could be caused by some other factors.

In comparison to the smooth surface of the original PCL film in Fig. 2f, PS films show much rougher surface in Fig. S11. It is known that the formed Cu-BHT layer migrates from the liquid-liquid interface to the substrate by removing the excess solutions during spin-coating. Ideally, the Cu-BHT layer can cover a smooth substrate completely, but it tends to be broken on substrates with a rough surface. This might explain why the Cu/BHT layers are broken on the PS surface in Fig. S11 but keep complete on the PCL surface in Fig. 2f. Therefore, both the conductivity and stability of Cu/BHT on PS are worse than those on PCL.

According to our findings, the initial and long-term conductivity of Cu-BHT on flexible substrates can be potentially ascribed to two crucial mechanisms as illustrated in Fig. 2g: namely the molecular movement inside the polymer and the fusion of polymers at the interface. First, the internal mobility caused by the low T_g makes the polymer an unstable substrate for the Cu-BHT. The molecular movement inside the polymer substrate may lead to the formation of a cracked Cu-BHT layer, resulting in its bad initial and long-term stability. All soft materials showing similar properties as PDMS and PU, are not suitable to serve as substrates for Cu-BHT. Second, the fusion of polymer substrates and Cu-BHT at the interface caused by the solvent solubility might enable the formation of embedded Cu-BHT/substrate layer as a single and stable entity and further the excellent conductivity and long-term stability. Therefore, the matching principle of polymer substrates and solvents could be one of the key factors contributing to the conductivity stability of the 2D Cu-MOFs. Besides, another possible factor—surface roughness—may affect a bit by leading to the formation of broken Cu-BHT, but it is not as crucial as the other two factors. In this case, the criteria for the selection of ideal substrates for Cu-BHT or other conductive 2D MOFs can be summarized as: polymer plastics with a high T_g (compared to the operating/ambient temperature), excellent dissolution ability (depending on the solvent of MOFs), and a smooth surface (helpful but not crucial).

To investigate its practical viability in flexible and wearable devices, Cu-BHT is further considered as the electrode of TENGs, and the efficiency of energy harvesting from water droplets and human motions is assessed. As shown in Fig. 3a and Fig. S12a, the flexible TENG is fabricated with PCL as the substrate, Cu-BHT as the electrode, and another polymer as the top-surface. It is noted that a thin and narrow layer of sliver is added as the top-electrode when harvesting water droplets energy, because two-electrode droplet-TENGs have recently been reported to show much higher output than single-electrode droplet-TENGs [31–33]. Although the working mechanism of the two-electrode mode

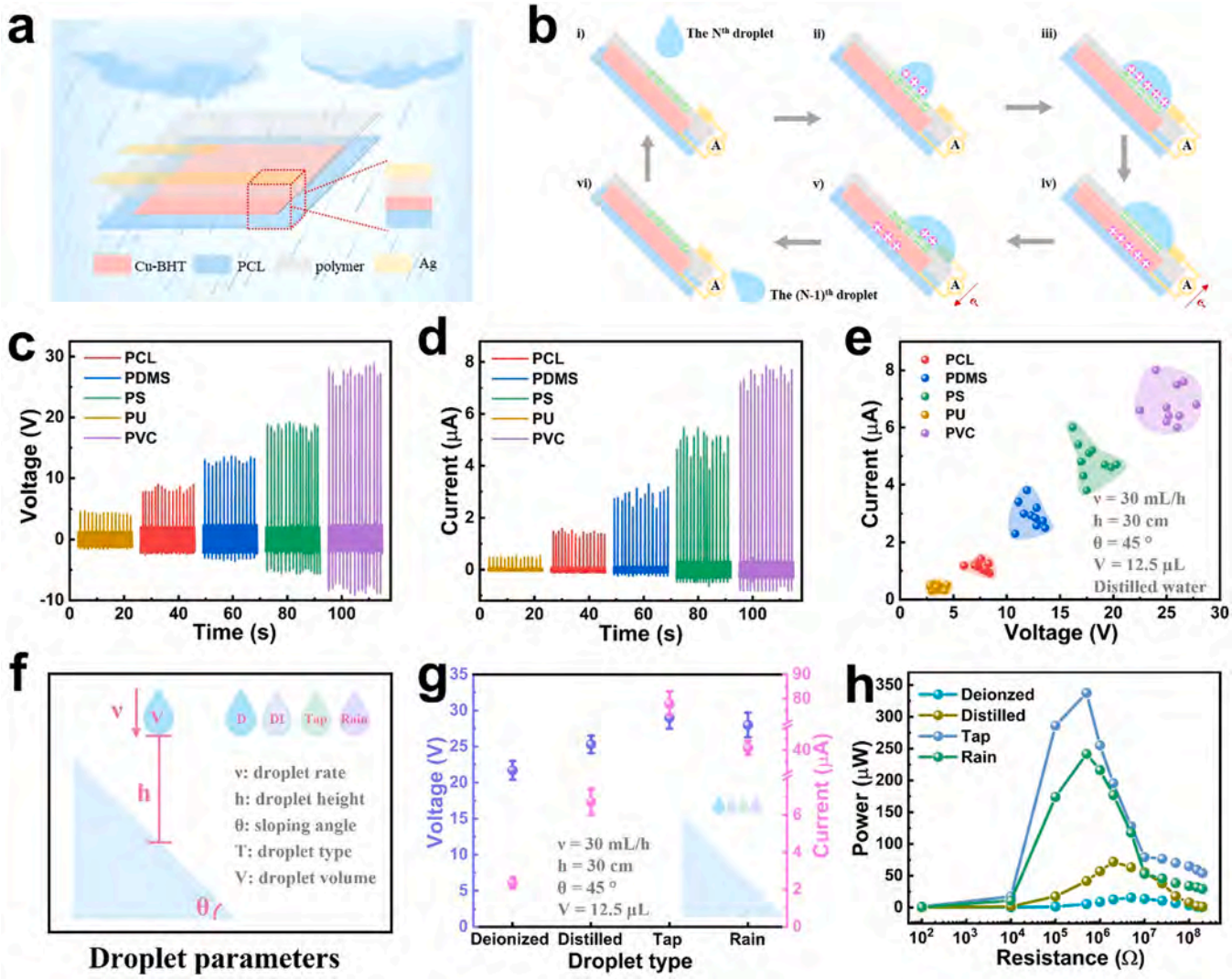

Fig. 3. Cu-BHT-based TENGs for water droplets energy harvesting: **a** schematic diagram of the PCL/Cu-BHT/polymer TENG for harvesting rain energy, **b** working principle of the two-electrode TENG for droplets energy harvesting, **c-e** effect of top surface on the device output, **f** droplet parameters that may affect the device output, and effects of the droplet types on **g** device output and **h** generated power in a load resistance range of 100 Ω – 200 MΩ.

has been explored in water droplet energy harvesting, the conclusion is still not clear. Nevertheless, whether the droplet is charged or forms an electric double layer before/after dripping should not affect the nature of triboelectricity between the device and the droplet. Therefore, we explored the potential working principle of two-electrode droplet TENG by focusing on the solid-liquid interface between the device surface and droplets.

It is noted that, the analysis of the schematic working mechanism in Fig. 3b starts after some opposite charges have already been accumulated on the top-surface by previous droplets. Therefore, when the N^{th} droplet drips and spreads on the device (Fig. 3b(i-iii)), the accumulated negative charges on the top-surface attract the positive charges inside the droplet to form a charge equilibrium at the liquid-solid interface. As soon as the droplet gets in contact with the top electrode (Fig. 3b(iv)), directional and rapid charge transfer occurs between electrodes to neutralize the induced positive charges in the droplet [31,32]. Consequently, an abrupt current signal is observed as shown in Fig. S13. As the droplet slides (Fig. 3b(v)), electrons generally flow back from the top electrode to the botto -electrode to get a final balance between the electrodes, and thus generate an opposite current. As the "leaving" process of a droplet needs a longer time than its "contacting" process, the obtained opposite signal is much wider and shorter despite the same/similar amounts of transferred charges (Fig. S13). Since the contact areas among the droplet and the top-surface/top-electrode change constantly, a slight fluctuation between the positive and negative charges could potentially happen at this stage [32]. After the droplet leaves the device (Fig. 3b(vi)), there will be no charge difference between the electrodes but only the accumulated negative charges left on the top-surface awaiting the next droplet.

Considering the hydrophobicity and tribo-negative property, the five polymer films of PCL, PDMS, PS, PU, and PVC are also selected as the top-surface of the device to harvest energy from water droplets. As shown in Fig. 3c-e, the voltage and current of these devices exhibit an increasing order of: PU < PCL < PDMS < PS < PVC. The best performance of PVC-based device can be attributed to the biggest triboelectric charge density as reported in Zou et al.'s work [34]. With the aid of the optimal PCL/Cu-BHT/PVC TENG, the influence of the droplet parameters such as droplet height, rate, type, as well as sloping angle on the device output is investigated (Fig. 3f). Noted that the droplet volume is fixed at 12.5 μL in this work to simulate the real rain situation for most cases. As shown in Fig. S12b, with the droplet height is increased from 2.5 cm to 15 cm, a linear increase in the device output is observed. This mainly results from the higher height causing the bigger gravity impact, and therefore the larger contact and spreading area of the droplet. Further increase of the droplet height barely affects the output, contributing to the fully spreading droplet when the height is above 15 cm. On the other hand, there is no apparent change in both voltage and current by changing the droplet rate in a large range of 15–180 mL/h (Fig. S12c). Theoretically, the output should be the same if only the droplet is in full contact with the device surface. Similarly, the sloping angle seems to have minimal impact on the output, although Fig. S12d shows a slight increase first and then a slight decrease at the angle range of 15–75°. These results indicate the wide tolerance and high practical potential of the device in different situations.

To further assess the viability of Cu-BHT-based devices in practical situations, different types of water are considered as droplet sources. A voltage increase is observed in Fig. 3g when deionized water is changed to distilled water, tap water, and rainwater. Interestingly, a more obvious increase in current is obtained by replacing distilled water with other types of droplets. Therefore, an apparent difference in the rectified output and the generated power among various droplet types in a wide resistance load range are also observed in Fig. S14 and Fig. 3h, where the power generated by tap water or rain droplets is hundreds of microwatts but that of deionized or distilled droplets is only tens of microwatts. To figure out the potential reasons causing this phenomenon, the conductivity and pH values of the four types of water were evaluated and the results are shown in Fig. S15. Obviously, the overall output increase mainly stems from higher conductivity rendered by the impurities in water rather than pH. It is believed that faster directional charge transfer in the presence of impure ions is the main reason leading to the shaper current signals, but the exact mechanism requires further in-depth studies.

The flexible properties of the developed Cu-BHT films and devices have been investigated qualitatively and quantitatively and discussed in detail in the supporting information (Fig. S16 and Fig. S17). Given its structure flexibility and portability, the developed PCL/Cu-BHT/PVC TENG can be potentially installed not only on roofs, umbrellas, as well as raincoats for water droplets energy harvesting, but also directly on the human bodies for biomechanical energy harvesting as schematic in Fig. 4a. Therefore, as a further demonstration, the device is attached to either the back of a hand (inset of Fig. 4b) or everyday clothes (inset of Fig. 4d) to harvest energy from human motions. It is observed in Fig. 4b, c that when the index finger taps the device gently, a voltage of ~22 V and a current of ~5 μA are produced indicative of the high sensitivity of the PCL/Cu-BHT/PVC TENG to human motions. Since cotton is the most popular clothing for everyday clothes, the person wearing a cotton glove when tapping the device is also tested. As shown in Fig. S18, a voltage of ~10 V and a current of ~1.5 μA are generated every time the cotton glove comes in contact and then gets separated from the device. This demonstrates the flexible device can be worn at any position of a human being wherever it has a chance to get contact with the human skin or clothes, indicating its wide usage range on human motions energy harvesting and detecting. Moreover, the device can also be worn on human clothes, in case some people may feel unsafe or uncomfortable having an electronic device directly on their skin. As shown in the inset of Fig. 4d, our device is worn on the clothes on the side of the waist. When the person walks or runs, it is inevitable that the arm will rub against the device forth and back. Therefore, alternating electrical signals will also be generated and further detect the walking/running steps.

To achieve the practical usage of the generated electricity from human motions, a rectifier and capacitor are added to the circuit (Fig. 4f) to transfer the output from alternating signals to direct signals and store the generated electricity, respectively. As shown in Fig. 4g and Video S1, ten LEDs can be lit every time when the device is gently tapped by the index finger. By continuously tapping the device 20 times, the generated electricity can be stored in a 1 μF capacitor to power a LED for one second as shown in Fig. 4h and Video S2. Therefore, the developed Cu-BHT device is very versatile being able to not only monitor human motions but also generate useful electricity by harvesting wasted human motions in their daily activities.

Supplementary material related to this article can be found online at doi:10.1016/j.nanoen.2023.108427.

Supplementary material related to this article can be found online at doi:10.1016/j.nanoen.2023.108427.

3. Conclusions

In this work, the underlying reasons leading to the difference in the initial conductivity and long-term stability of 2D MOFs on different substrates are fully investigated. First, the molecular movement inside the polymer due to a lower T_g makes it a potentially unstable substrate for Cu-BHT, which might lead to the formation of cracked layers with conductivity instability. Second, the fusion of the polymer and Cu-BHT due to the solvent solubility could be crucial to the conductivity stability resulting from the formation of embedded composite layers at the interface. Besides, the surface smoothness helps to conformal and complete coverage of the Cu-BHT layer and broken Cu-BHT layers with slightly lower conductivity can be produced on rough substrates. By selecting the suitable substrate, Cu-BHT forms an excellent electrode in flexible/wearable devices. For example, the developed Cu-BHT-based TENG is very efficient in harvesting water droplets and human motion energy for wearable sensing and electronics powering. This work reveals

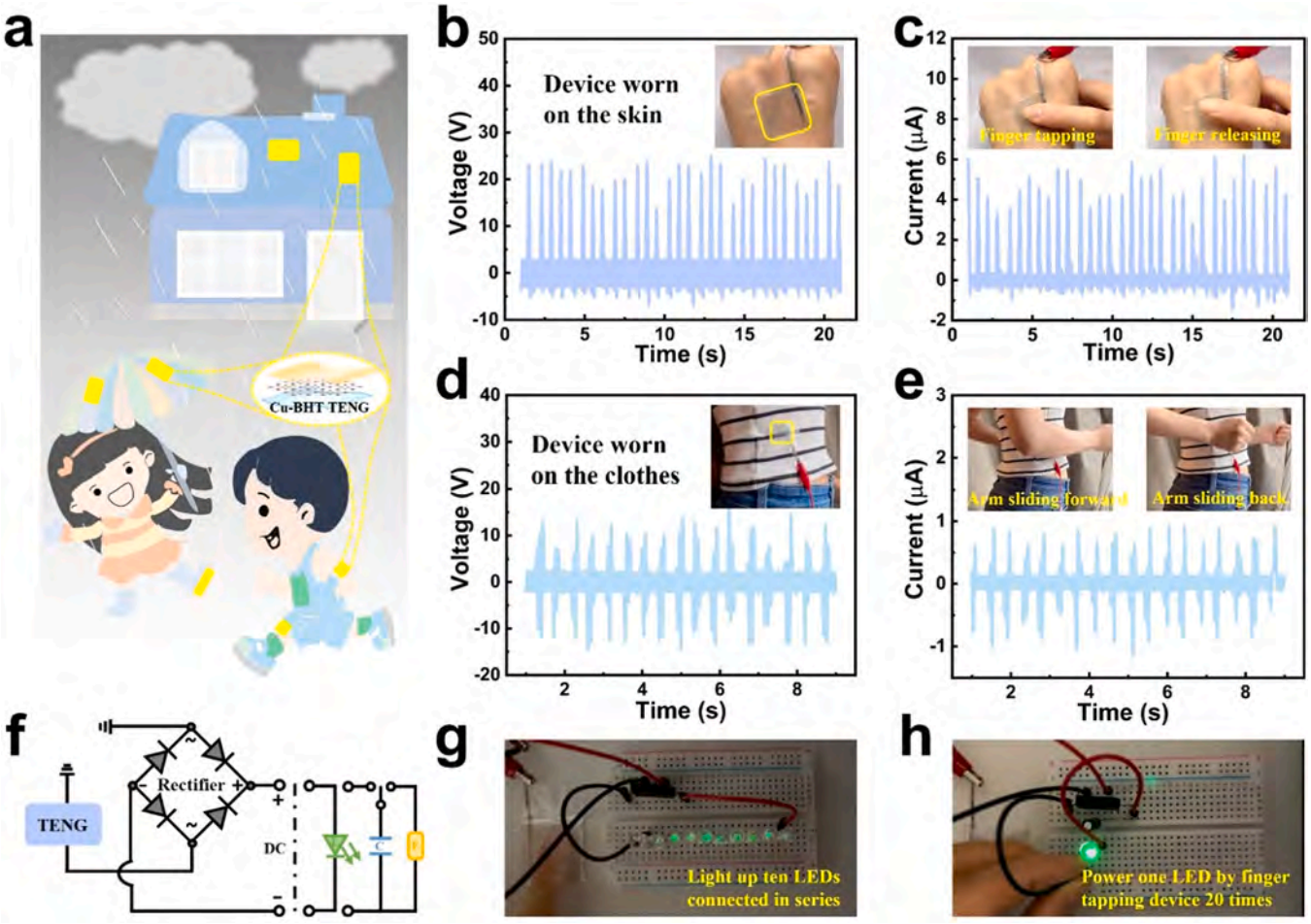

Fig. 4. Cu-BHT-based TENGs for human motion energy harvesting: a schematic diagram of the PCL/Cu-BHT/PVC TENG putting on house roof, umbrella, human clothes, as well as human body for water droplets and human motions energy harvesting, **b** voltage and **c** current generated by tapping the index finger on the device worn on one hand, **d** voltage and **e** current generated by rubbing the arm against the device worn on clothes during exercise, **f** schematic diagram of the circuit with external loads such as LEDs, capacitors and small electronics, **g** ten LEDs connected in series lit up finger tapping the device, and **h** a green LED powered by a 1 μF capacitor with finger tapping the device for 20 times.

the potentially underlying factors concerning the conductivity stability of Cu-BHT and fundamental rules for the choice of flexible substrates for 2D MOFs, which advances the understanding and applications of conductive MOFs as electrodes in next-generation flexible and wearable electronics.

CRediT authorship contribution statement

Yinghong Wu: Conceptualization; Data curation; Formal analysis; Investigation; Methodology; Validation; Writing – original draft, Yang Luo: Conceptualization; Data curation; Formal analysis; Methodology; Software; Validation; Writing – original draft, Paul K. Chu: Funding acquisition; Writing – review & editing, Carlo Menon: Funding acquisition; Resources; Supervision; Writing – review & editing.

Declaration of Competing Interest

The authors declare that they have no known competing financial interests or personal relationships that could have appeared to influence the work reported in this paper.

Data availability

Data will be made available on request.

Acknowledgments

This work was supported by City University of Hong Kong Donation Research Grant (DON-RMG, No. 9229021) and City University of Hong Kong Strategic Research Grant (SRG, No. 7005505). The authors would like to thank Dr. Tyler J. Cuthbert and Dr. Sunil Kumar Sailapu for the discussion about polymer properties and charge transfer mechanism.

Appendix A. Supporting information

Supplementary data associated with this article can be found in the online version at doi:10.1016/j.nanoen.2023.108427.

References

[1] S. Xu, S. Chansai, C. Stere, B. Inceesungvorn, A. Goguet, K. Wangkawong, S.F. R. Taylor, N. Al-Janabi, C. Hardacre, P.A. Martin, X. Fan, Sustaining metal–organic frameworks for water–gas shift catalysis by non-thermal plasma, Nat. Catal. 2 (2019) 142–148, https://doi.org/10.1038/s41929-018-0206-2.
[2] I. Abánades Lázaro, C.J.R. Wells, R.S. Forgan, Multivariate modulation of the Zr MOF UiO-66 for defect-controlled combination anticancer drug delivery, Angew. Chem. Int. Ed. 59 (2020) 5211–5217, https://doi.org/10.1002/anie.201915848.
[3] Y.-M. Jo, Y.K. Jo, J.-H. Lee, H.W. Jang, I.-S. Hwang, D.J. Yoo, MOF-based vhemiresistive gas Sensors: toward new functionalities, Adv. Mater. (2022) 2206842, https://doi.org/10.1002/adma.202206842.
[4] M.R. Lukatskaya, D. Feng, S.-M. Bak, J.W.F. To, X.-Q. Yang, Y. Cui, J.I. Feldblyum, Z. Bao, Understanding the mechanism of high capacitance in nickel hexaaminobenzene-based conductive metal–organic frameworks in aqueous

electrolytes, ACS Nano 14 (2020) 15919–15925, https://doi.org/10.1021/acsnano.0c07292.
[5] G. Khandelwal, A. Chandrasekhar, N.P. Maria Joseph Raj, S.-J. Kim, Metal–organic framework: a novel material for triboelectric nanogenerator–based self-powered sensors and systems, Adv. Energy Mater. 9 (2019) 1803581, https://doi.org/10.1002/aenm.201803581.
[6] Y. Guo, Y. Cao, Z. Chen, R. Li, W. Gong, W. Yang, Q. Zhang, H. Wang, Fluorinated metal-organic framework as bifunctional filler toward highly improving output performance of triboelectric nanogenerators, Nano Energy 70 (2020), 104517, https://doi.org/10.1016/j.nanoen.2020.104517.
[7] S. Shen, J. Yi, Z. Sun, Z. Guo, T. He, L. Ma, H. Li, J. Fu, C. Lee, Z.L. Wang, Human machine interface with wearable electronics using biodegradable triboelectric films for calligraphy practice and correction, Nano-Micro Lett. 14 (2022) 225, https://doi.org/10.1007/s40820-022-00965-8.
[8] Z. Shao, J. Chen, K. Gao, Q. Xie, X. Xue, S. Zhou, C. Huang, L. Mi, H. Hou, A double-helix metal-chain metal-organic framework as a high-output triboelectric nanogenerator material for self-powered anticorrosion, Angew. Chem. Int. Ed. (2022), e202208994, https://doi.org/10.1002/anie.202208994.
[9] G. Khandelwal, N.P. Maria Joseph Raj, S.-J. Kim, Zeolitic Imidazole framework: metal–organic framework subfamily members for triboelectric nanogenerators, Adv. Funct. Mater. 30 (2020) 1910162, https://doi.org/10.1002/adfm.201910162.
[10] G. Khandelwal, N.P. Maria Joseph Raj, S.-J. Kim, ZIF-62: a mixed linker metal–organic framework for triboelectric nanogenerators, J. Mater. Chem. A 8 (2020) 17817–17825, https://doi.org/10.1039/D0TA05067A.
[11] M.T. Rahman, S.S. Rana, M.A. Zahed, S. Lee, E.-S. Yoon, J.Y. Park, Metal-organic framework-derived nanoporous carbon incorporated nanofibers for high-performance triboelectric nanogenerators and self-powered sensors, Nano Energy 94 (2022), 106921, https://doi.org/10.1016/j.nanoen.2022.106921.
[12] R. Wen, R. Feng, B. Zhao, J. Song, L. Fan, J. Zhai, Controllable design of high-efficiency triboelectric materials by functionalized metal—organic frameworks with a large electron-withdrawing functional group, Nano Res (2022), https://doi.org/10.1007/s12274-022-4731-6.
[13] Q. Fu, Y. Liu, T. Liu, J. Mo, W. Zhang, S. Zhang, B. Luo, J. Wang, Y. Qin, S. Wang, S. Nie, Air-permeable cellulosic triboelectric materials for self-powered healthcare products, Nano Energy 102 (2022), 107739, https://doi.org/10.1016/j.nanoen.2022.107739.
[14] X. Huang, P. Sheng, Z. Tu, F. Zhang, J. Wang, H. Geng, Y. Zou, C. Di, Y. Yi, Y. Sun, W. Xu, D. Zhu, A two-dimensional π–d conjugated coordination polymer with extremely high electrical conductivity and ambipolar transport behaviour, Nat. Commun. 6 (2015) 7408, https://doi.org/10.1038/ncomms8408.
[15] X. Zhang, Y. Zhou, B. Cui, M. Zhao, F. Liu, Theoretical discovery of a superconducting two-dimensional metal–organic framework, Nano Lett. 17 (2017) 6166–6170, https://doi.org/10.1021/acs.nanolett.7b02795.
[16] M. Li, Z. Wu, M. Zheng, H. Chen, T. Gould, S. Zhang, First-principles exploration of 2D benzenehexathiolate coordination nanosheets for broadband electrochromic devices, Adv. Funct. Mater. (2022) 2202763, https://doi.org/10.1002/adfm.202202763.
[17] X. Huang, S. Zhang, L. Liu, L. Yu, G. Chen, W. Xu, D. Zhu, Superconductivity in a copper(II)-based coordination polymer with perfect Kagome structure, Angew. Chem. Int. Ed. 57 (2018) 146–150, https://doi.org/10.1002/anie.201707568.
[18] T. Takenaka, K. Ishihara, M. Roppongi, Y. Miao, Y. Mizukami, T. Makita, J. Tsurumi, S. Watanabe, J. Takeya, M. Yamashita, K. Torizuka, Y. Uwatoko, T. Sasaki, X. Huang, W. Xu, D. Zhu, N. Su, J.-G. Cheng, T. Shibauchi, K. Hashimoto, Strongly correlated superconductivity in a copper-based metal-organic framework with a perfect kagome lattice, Sci. Adv. 7 (2021) eabf3996, https://doi.org/10.1126/sciadv.abf3996.
[19] X. Huang, H. Yao, Y. Cui, W. Hao, J. Zhu, W. Xu, D. Zhu, Conductive copper benzenehexathiol coordination polymer as a hydrogen evolution catalyst, ACS Appl. Mater. Interfaces 9 (2017) 40752–40759, https://doi.org/10.1021/acsami.7b14523.
[20] Z. Jin, J. Yan, X. Huang, W. Xu, S. Yang, D. Zhu, J. Wang, Solution-processed transparent coordination polymer electrode for photovoltaic solar cells, Nano Energy 40 (2017) 376–381, https://doi.org/10.1016/j.nanoen.2017.08.028.
[21] Z. Wu, D. Adekoya, X. Huang, M.J. Kiefel, J. Xie, W. Xu, Q. Zhang, D. Zhu, S. Zhang, Highly conductive two-dimensional metal–organic frameworks for resilient lithium storage with superb rate capability, ACS Nano 14 (2020) 12016–12026, https://doi.org/10.1021/acsnano.0c05200.
[22] X. Chen, J. Dong, K. Chi, L. Wang, F. Xiao, S. Wang, Y. Zhao, Y. Liu, Electrically conductive metal–organic framework thin film-based on-chip micro-biosensor: a platform to unravel surface morphology-dependent biosensing, Adv. Funct. Mater. 31 (2021) 2102855, https://doi.org/10.1002/adfm.202102855.
[23] L. Wang, X. Chen, Z. Yi, R. Xu, J. Dong, S. Wang, Y. Zhao, Y. Liu, Facile synthesis of conductive metal−organic frameworks nanotubes for ultrahigh-performance flexible NO sensors, Small Methods 6 (2022) 2200581, https://doi.org/10.1002/smtd.202200581.
[24] X. Chen, Y. Lu, J. Dong, L. Ma, Z. Yi, Y. Wang, L. Wang, S. Wang, Y. Zhao, J. Huang, Y. Liu, Ultrafast in situ synthesis of large-area conductive metal–organic frameworks on substrates for flexible chemiresistive sensing, ACS Appl. Mater. Interfaces 12 (2020) 57235–57244, https://doi.org/10.1021/acsami.0c18422.
[25] Y. Jin, Y. Li, Y. Sun, M. Zhu, Z. Li, L. Liu, Y. Zou, C. Liu, Y. Sun, W. Xu, Facile synthesis, precise species control and chemical transformation of highly conducting organic metal chalcogenides CuxBHT (BHT = benzenehexathiol; x = 3, 4, and 5.5), J. Mater. Chem. C 10 (2022) 2711–2717, https://doi.org/10.1039/D1TC03614A.
[26] F. Li, X. Zhang, X. Liu, M. Zhao, Novel conductive metal–organic framework for a high-performance lithium–sulfur battery host: 2D Cu-benzenehexathial (BHT), ACS Appl. Mater. Interfaces 10 (2018) 15012–15020, https://doi.org/10.1021/acsami.8b00942.
[27] L. Sun, M.G. Campbell, M. Dincă, Electrically conductive porous metal–organic frameworks, Angew. Chem. Int. Ed. 55 (2016) 3566–3579, https://doi.org/10.1002/anie.201506219.
[28] I. Stassen, N. Burtch, A. Talin, P. Falcaro, M. Allendorf, R. Ameloot, An updated roadmap for the integration of metal–organic frameworks with electronic devices and chemical sensors, Chem. Soc. Rev. 46 (2017) 3185–3241, https://doi.org/10.1039/C7CS00122C.
[29] T. Kambe, R. Sakamoto, T. Kusamoto, T. Pal, N. Fukui, K. Hoshiko, T. Shimojima, Z. Wang, T. Hirahara, K. Ishizaka, S. Hasegawa, F. Liu, H. Nishihara, Redox control and high conductivity of mickel bis(dithiolene) xomplex π-nanosheet: a potential organic two-dimensional topological insulator, J. Am. Chem. Soc. 136 (2014) 14357–14360, https://doi.org/10.1021/ja507619d.
[30] R. Toyoda, N. Fukui, D.H.L. Tjhe, E. Selezneva, H. Maeda, C. Bourgès, C.M. Tan, K. Takada, Y. Sun, I. Jacobs, K. Kamiya, H. Masunaga, T. Mori, S. Sasaki, H. Sirringhaus, H. Nishihara, Heterometallic benzenehexathiolato coordination nanosheets: periodic structure improves crystallinity and electrical conductivity, Adv. Mater. 34 (2022) 2106204, https://doi.org/10.1002/adma.202106204.
[31] W. Xu, H. Zheng, Y. Liu, X. Zhou, C. Zhang, Y. Song, X. Deng, M. Leung, Z. Yang, R. X. Xu, Z.L. Wang, X.C. Zeng, Z. Wang, A droplet-based electricity generator with high instantaneous power density, Nature 578 (2020) 392–396, https://doi.org/10.1038/s41586-020-1985-6.
[32] Q. Zhang, Y. Li, H. Cai, M. Yao, H. Zhang, L. Guo, Z. Lv, M. Li, X. Lu, C. Ren, P. Zhang, Y. Zhang, X. Shi, G. Ding, J. Yao, Z. Yang, Z.L. Wang, A single-droplet electricity generator achieves an ultrahigh output over 100 V without pre-charging, Adv. Mater. 33 (2021) 2105761, https://doi.org/10.1002/adma.202105761.
[33] C. Ye, D. Liu, X. Peng, Y. Jiang, R. Cheng, C. Ning, F. Sheng, Y. Zhang, K. Dong, Z. L. Wang, A Hydrophobic self-repairing power textile for effective water droplet energy harvesting, ACS Nano 15 (2021) 18172–18181, https://doi.org/10.1021/acsnano.1c06985.
[34] H. Zou, Y. Zhang, L. Guo, P. Wang, X. He, G. Dai, H. Zheng, C. Chen, A.C. Wang, C. Xu, Z.L. Wang, Quantifying the triboelectric series, Nat. Commun. 10 (2019) 1427, https://doi.org/10.1038/s41467-019-09461-x.

Supporting Information

Revealing the conductivity stability of 2D Cu-MOFs as flexible electrodes: demonstration of triboelectric nanogenerators

Yinghong Wu[a,], Yang Luo[b,]*, Paul K. Chu[b], and Carlo Menon[a,]**

[a]Biomedical and Mobile Health Technology Lab, Department of Health Sciences and Technology, ETH Zurich, Zurich, Switzerland.

[b]Department of Physics, City University of Hong Kong, Hong Kong, China.

*****Corresponding authors: yinghong.wu@hest.ethz.ch, yluo24-c@my.cityu.edu.hk and carlo.menon@hest.ethz.ch

1. Experimental section

Materials: copper chloride ($CuCl_2$, Sigma-Aldrich), 37% hydrochloric acid (HCl, Sigma-Aldrich), 1,2,3,4,5,6-benzenehexathiol (BHT, BLD Pharmatech) deionized water (DI water, 18.2 MΩ), chlorobenzene (CB, Sigma-Aldrich), polycaprolactone (PCL, Sigma-Aldrich), polydimethylsiloxane (PDMS, DC184), polystyrene (PS, Sigma-Aldrich), polyurethane (PU, thermoplastic, Sigma-Aldrich), polyvinyl chloride (PVC, Sigma-Aldrich).

Synthesis of conductive Cu-BHT films: Droplets of $CuCl_2$ (5 mM) acidic solution (HCl, pH=1) were dripped on a plasma-treated substrate (FEMTO, a low-pressure plasma system with an O_2 flow rate of 5 sccm for 3 min) until it covered the full surface. Then, droplets of BHT/CB (0.1 mM) solution were gently dripped on the $CuCl_2$ aqueous layer until it was fully covered by the BHT/CB layer. After leaving the interface reaction between Cu^{2+} and BHT for a few seconds (15-240 s depending on the needs), the spin coater was rotated at 500 rpm for 20 s and then 1500 rpms for 30 s to remove the remaining liquids on the substrate. Finally, a uniform and transparent film can be observed on the substrate.

***Fabrication of the MOFs-TENG*:** Droplets of polymer solution (PCL, PDMS, PS, PU, and PVC) were dripped and spin-coated on a clean glass at 1500 rpm for 20 s. After the solvent was evaporated in the oven at 80 °C, a clear and uniform polymer film was formed on the glass. Afterwards, a transparent and conductive Cu-BHT layer was spin-coated on the polymer/glass substrate following the synthesis procedure of conductive Cu-BHT film, followed by another layer of polymer film attaching on the top surface. Finally, the fabricated device was peeled off from the glass for further use. The schematic diagram and photograph of a typical device can be found in Fig. 3a and Fig. S10a to fully understand the TENG fabrication in this work.

Characterization and measurement: A fiber optic spectroscopy setup (including a light source (SLS201L/M, ThorLabs), a visible light spectrometer (CCS100/M, Thorlabs), optical fibers, and collimating lenses) was used to record the transmittance of the samples in the visible wavelength range. A scanning electron microscope (SEM, SU5000, HITACHI) and a transmission electron microscope (TEM, Talos F200X, FEI Tescan VEGA3) were used to observe the morphology of the samples. An X-ray diffractometer (XRD, X'pert Pro MPD, PANalytical) and an X-ray photoelectron spectroscope (XPS, ESCALAB 250Xi, Thermo Fisher) were used to identify the phase of the samples. A Raman spectrometer (inVia Reflex, Renishaw) and a Fourier transform infrared spectrometer (ATR-IR, ALPHA, Bruker) were used to investigate the functional group of the samples. An atomic force microscopy (AFM, FastScan, Bruker) was used to measure the surface morphology and film thickness of the samples. An electrodynamic test instrument (Electropuls E3000, Instron) was used to bend the samples at the radius of 5 mm for flexibility test. A potentiostat/galvanostat with integrated impedance analyzer (μStat-i 400, Metrohm DropSens) and a multimeter (Model 177, FLUKE) were used to measure the resistance of the samples. A pump (SKU300, InfusionONE) was used to control the dripping rate of the droplets. An oscilloscope (MDO34, Tektronix) with a high voltage probe (PR1050D, RIGOL) and a low-noise current preamplifier (SR570, Stanford Research Systems) were used to evaluate the output of the triboelectric devices.

2. Simulation and Calculation details

DFT calculation method: DFT calculation was conducted with the Vienna ab initio simulation package (VASP).[S1] The ion-electron interactions were calculated by the projector augmented wave (PAW) method.[S2] A generalized gradient approximation in the Perdew-

Burke-Ernzerhof (PBE) form[S3] was used and a cutoff energy of 450 eV was set for the plane-wave basis set. The convergence criteria for residual force and energy were set as 0.01 eV/Å and 10^{-5} eV, respectively. Brillouin-zone (BZ) integration was performed on a gamma k-point mesh with Gaussian smearing of 0.05 eV.[S4] To derive the density of states and band structure, the accuracy was improved by using a 2 × 2 × 1 Monkhorst-Pack k-point mesh.

3. Advantages of 2D Cu-MOFs

1) Self-assembly synthesis: 2D Cu-MOFs can be synthesized without strict and demanding reaction controls (realized at a fast self-assembly time of one to several seconds, mild liquid condition, and simple reaction vessel).

2) Tunable functional frameworks: 2D Cu-MOFs can be tuned through different strategies such as metal center valence, vacancies, doping, solvent environment, etc.

3) Designable morphologies: Based on the self-assembly feature, 2D Cu-MOFs can be shaped into a variety of morphologies such as nanorods, nanosheets, nanotubes, and even thin films.

4) Controllable 2D thin film: with the change in reaction time and solution concentration, the thickness and surface conductivity of the 2D Cu-MOFs can be easily tuned, which can satisfy different application needs.

5) Excellent electrical conductivity: owing to the high electron delocalization in 2D ultrathin regions derived from π-d conjugations, 2D Cu-MOFs show excellent theoretical conductivity that is comparable to metal and much higher than other flexible electrodes.

6) High transparency: 2D Cu-MOFs exhibit a high transmittance of 80-90%, which shows great application potential in electronic skins, smart screens, etc.

4. Supplemental Data and Analysis

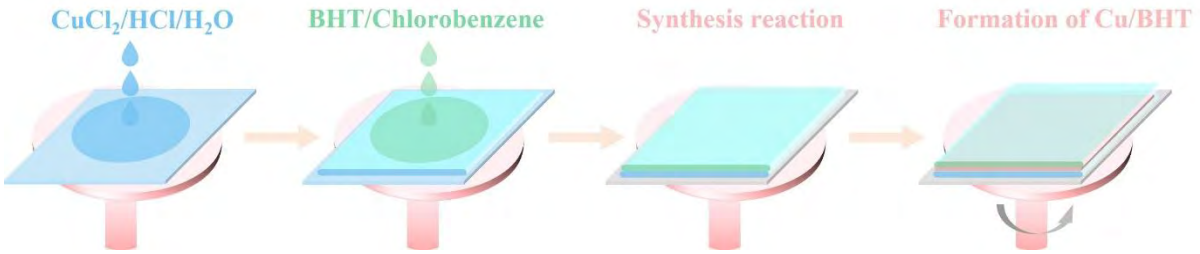

Fig. S1. Schematic diagram of the fabrication process of the Cu-BHT film.

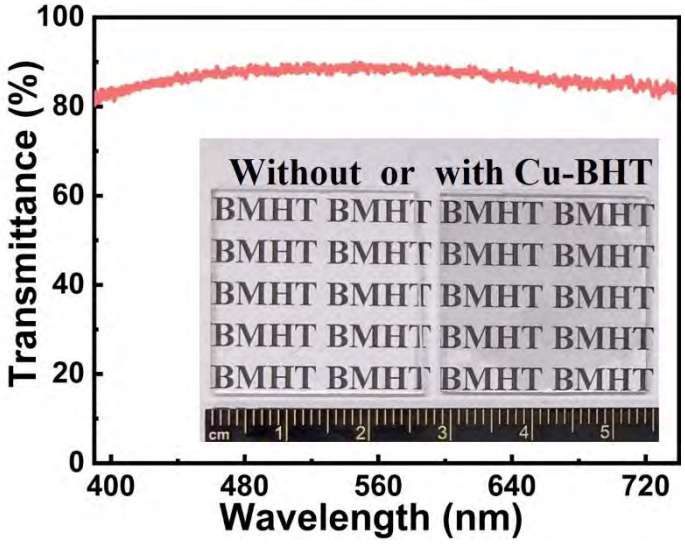

Fig. S2. Transmittance of the Cu-BHT layer, inset is the photograph of substrate with or without Cu-BHT layer.

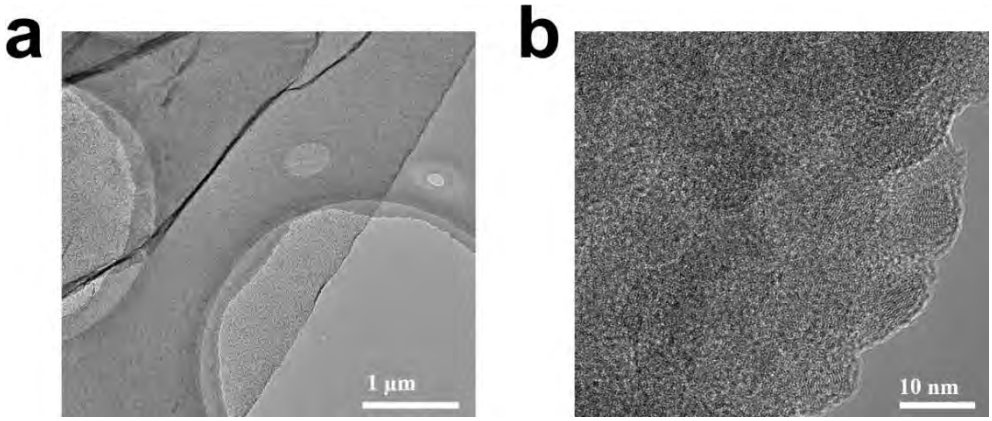

Fig. S3. a) TEM and b) HR-TEM images of Cu-BHT.

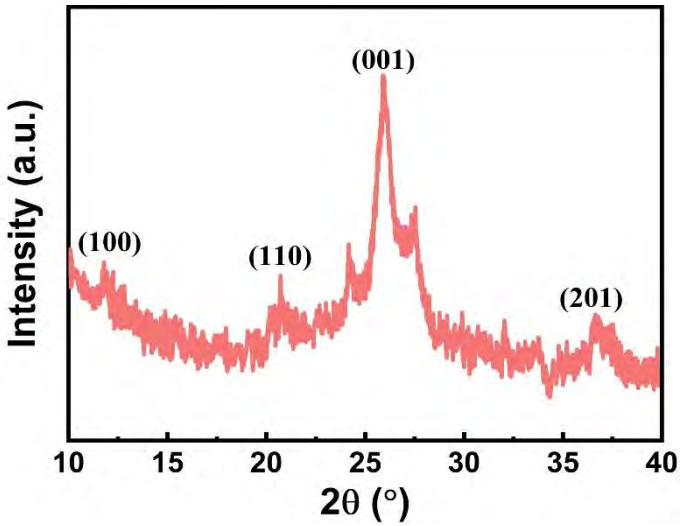

Fig. S4. XRD pattern of Cu-BHT.

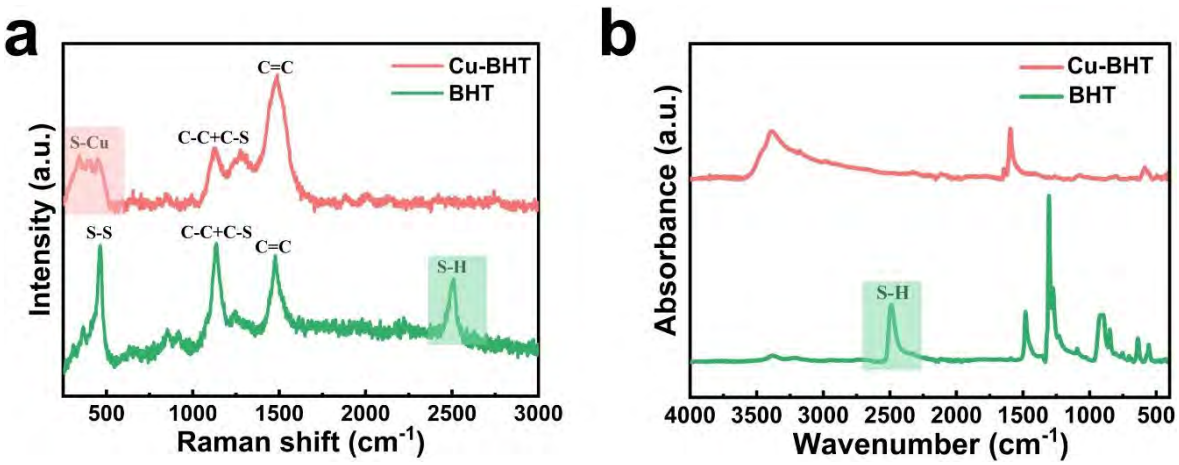

Fig. S5. a) Raman scattering spectra and b) ATR-IR spectra of BHT and Cu-BHT.

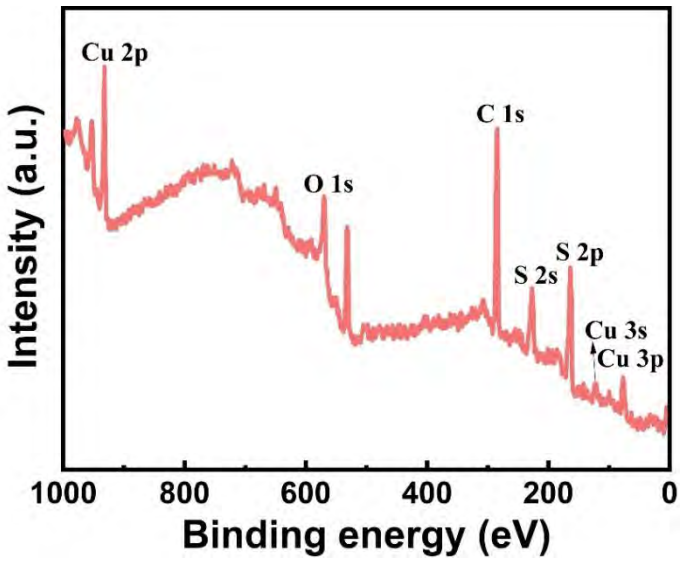

Fig. S6. XPS survey spectra of Cu-BHT.

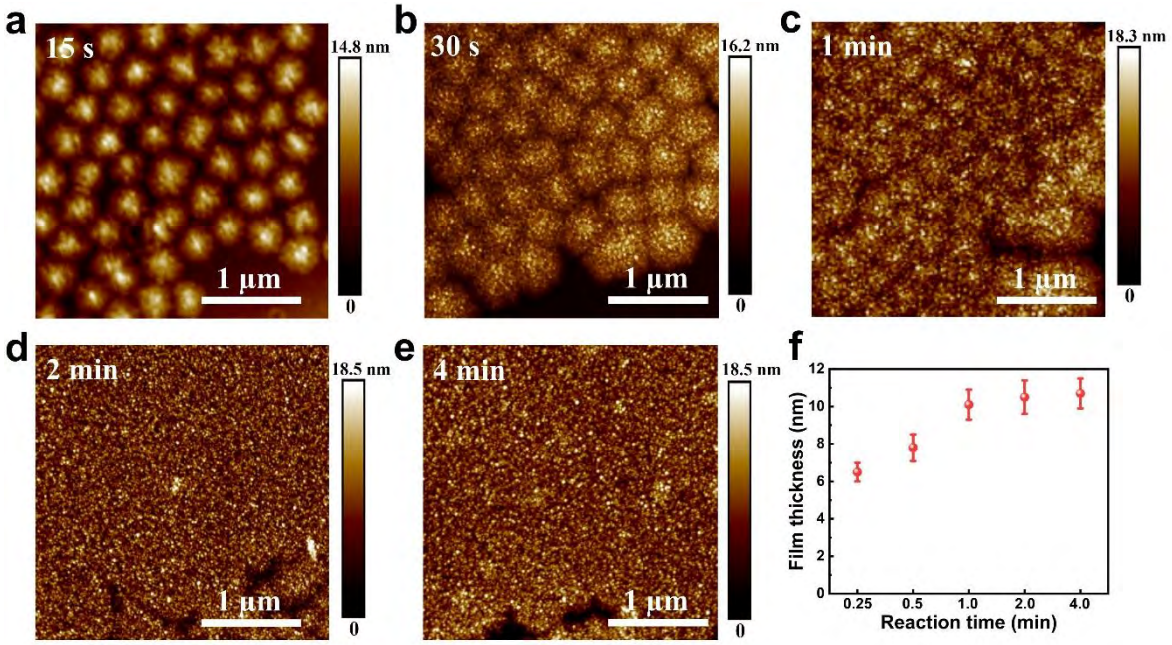

Fig. S7. AFM images of Cu-BHT films with the reaction time of a) 15 s, b) 30 s c) 1 min, d) 2 min and e) 4 min, and f) thickness of Cu-BHT film with the reaction time of 15 s – 4 min.

As shown in Fig. S8, no obvious difference was observed in the conductivity after bending Cu-BHT films with different reaction time or thickness for 0, 100, 500, and 1000 cycles, indicating that Cu-BHT films with different thicknesses show both excellent conductivity and flexibility.

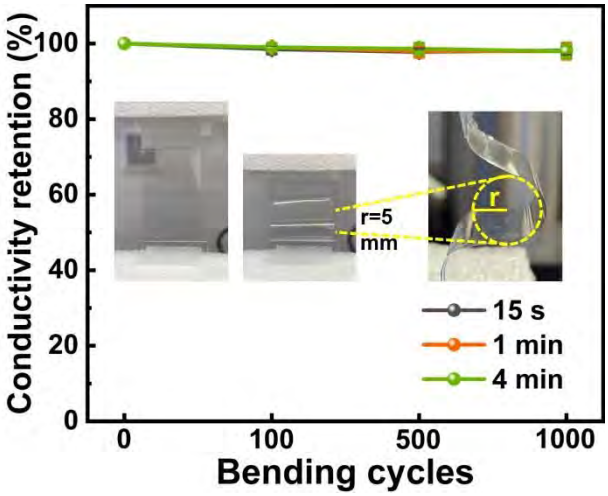

Fig. S8. Conductivity stability Cu-BHT films with different reaction time after bending at a radius of 5 mm for 0, 100, 500, 1000 cycles.

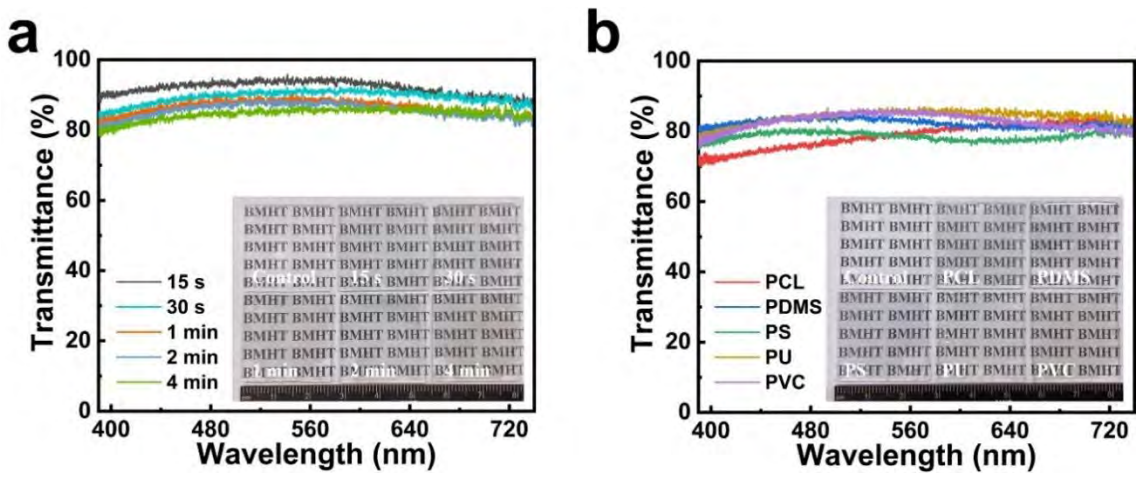

Fig. S9. Transmittance of Cu-BHT layers a) with different reaction time (15s, 30s, 1min, 2min, 4min) and b) with different polymer substrates (PCL, PDMS, PS, PU, PVC).

To further verify the potential fusion of Cu-BHT and polymer substrates, the effect of chlorobenzene immersion on the polymer substrate surfaces (Fig. S10b) and the effect of water rinse on the conductivity of the Cu-BHT/polymer films (Fig. S10c) were studied and compared. As shown in Fig. S10c, the conductivity of both Cu-BHT/PCL and Cu-BHT/PS almost kept the same before and after water rinse, indicating that a strong interaction occurs between Cu-BHT and PCL or PS. This interaction was caused by the solubility of PCL and PS in chlorobenzene (Fig. S10b, where nothing was left after PCL and PS films were put in chlorobenzene as they were completely dissolved). On the other hand, the conductivity changes of Cu-BHT/PDMS, Cu-BHT/PU, and Cu-BHT/PVC were much bigger as these substrates can not be dissolved by chlorobenzene (Fig. S10b) but only somehow swelled and therefore no interpenetration happened between them and Cu-BHT.

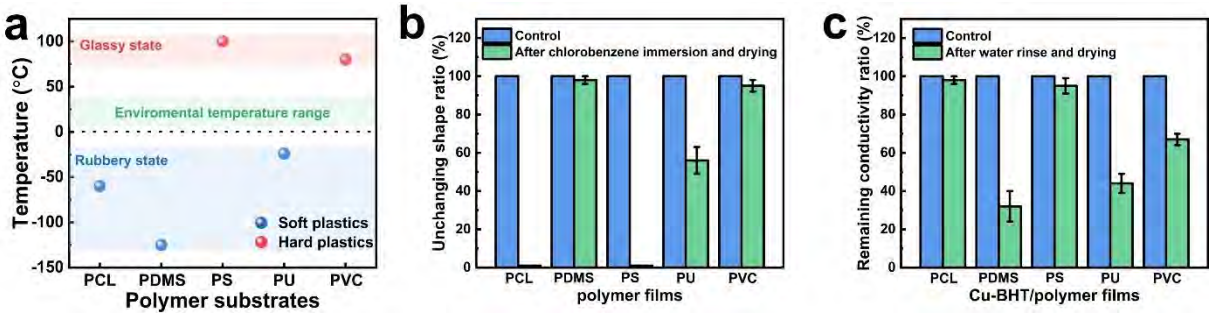

Fig. S10. Glass transition temperature of different polymers (PCL, PDMS, PS, PU, PVC), b) shape stability of polymer films after chlorobenzene immersion, and c) conductivity stability of Cu-BHT/polymer films before and after water rinse.

As shown in Fig. 2f and Fig. S11, the microstructures of various polymer films (PCL, PDMS, PS, PU, and PVC) and their corresponding Cu-BHT/polymer films are investigated and compared. It is found that, both PCL and PDMS films show a very smooth surface, but the microstructures of the formed Cu-BHT layers on these two polymer films are quite different. For example, an intact Cu-BHT layer with tiny wrinkles is formed on PCL, owing to the perfect fusion between Cu-BHT and PCL during the solvent evaporation process. However, a cracked Cu-BHT layer is generated on PDMS because of the internal molecular movement of PDMS resulting from the low glass transition temperature. A broken Cu-BHT layer on PS film is observed, which is mainly due to the surface roughness of the substrate. As for Cu-BHT/PU film, a lot of small pieces of Cu-BHT are formed on the surface, contributing to a first swelling and then shrinking phenomenon of PU responding to the solvent. No obvious difference was observed on PVC and Cu-BHT/PVC surfaces, attributing to its glassy property and smooth surface.

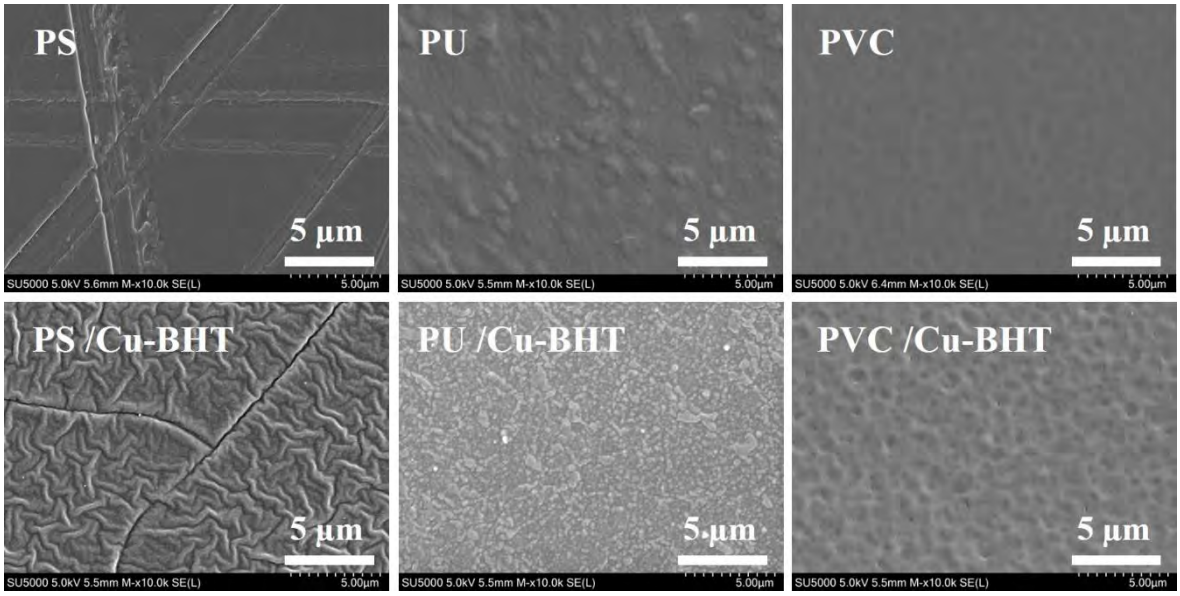

Fig. S11. SEM images of PS, PU and PVC films with or without covered Cu-BHT layer.

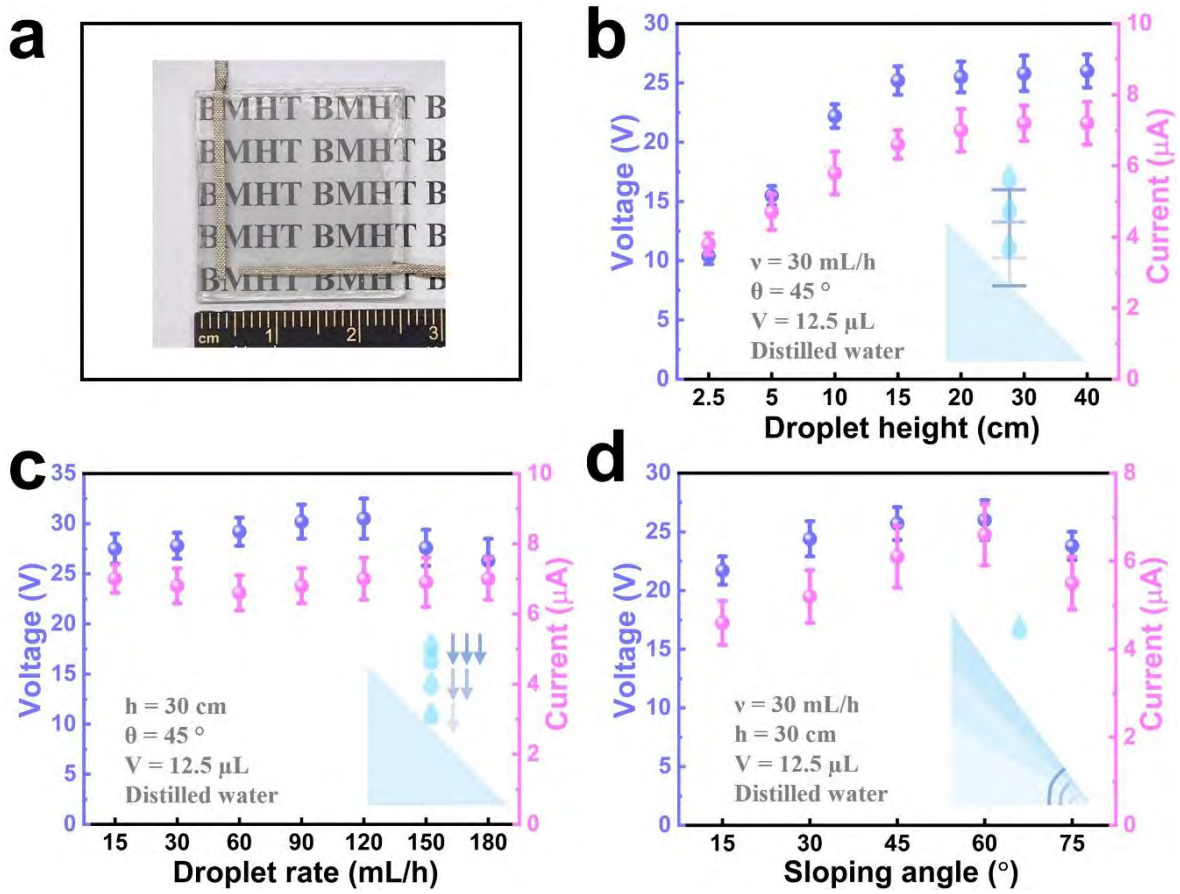

Fig. S12. a) Photograph of a typical PCL/Cu-BHT/PVC TENG device, b) effect of droplet height on the device output, c) effect of the droplet rate on the device output, and d) effect of the sloping angle on the device output.

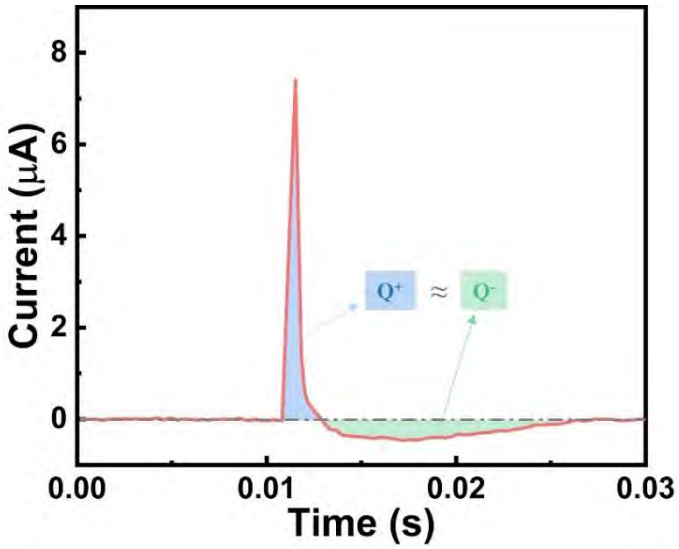

Fig. S13. The current signal of Cu-BHT-based TENG based on one single droplet.

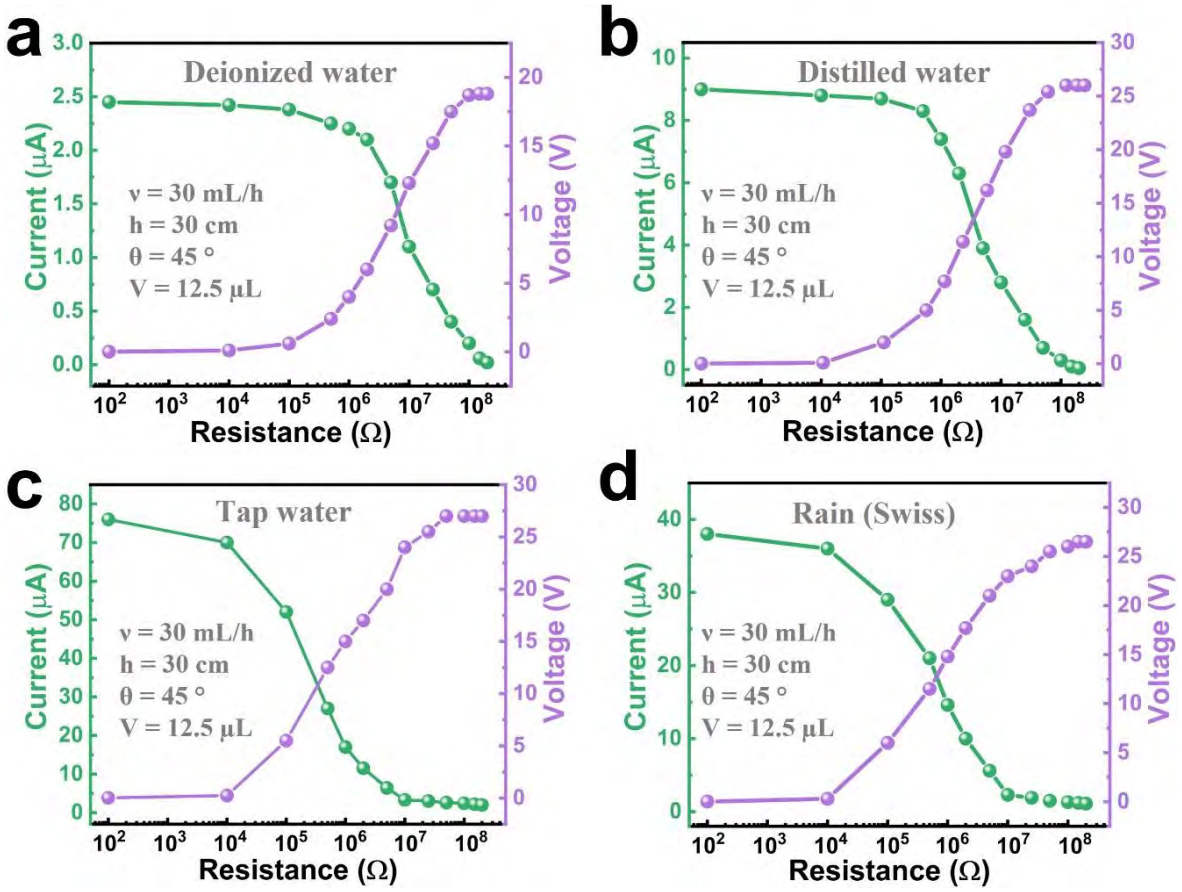

Fig. S14. Dependence of the output voltage and current density at the load resistance range of 100 Ω - 200 MΩ when using different water droplets: a) deionized water, b) distilled water, c) tap water, and d) rainwater in Swiss.

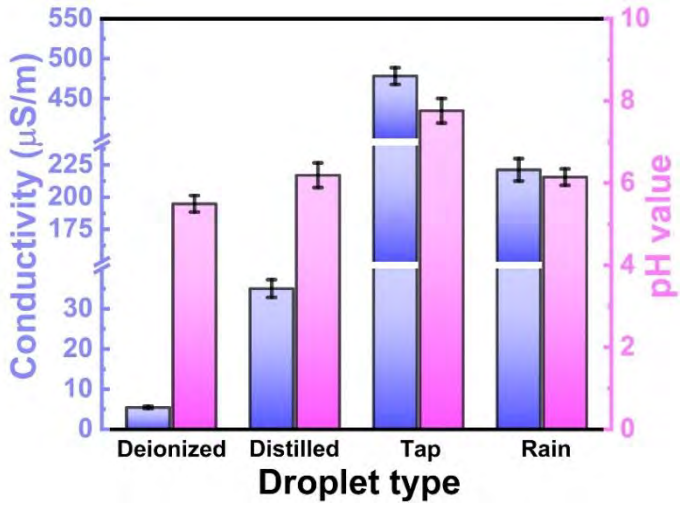

Fig. S15. Effect of the water types on the conductivity and pH values of droplets.

In addition to being directly worn on the human skin, the fabricated Cu-BHT TENG is capable to be wrapped around a pen with a diameter of 1 cm as shown in Fig. S16, showing the high flexibility of the Cu-BHT films/devices. To quantitatively evaluate the flexible properties, an Instron machine is used to constantly bend the Cu-BHT films/devices with the bending radius of 5 mm. As shown in Fig. S17, the conductivity of both Cu-BHT/PCL and Cu-BHT/PVC films exhibits negligible change after 100, 500, 1000 bending cycles. Moreover, the output voltage and current of PCL/Cu-BHT/PVC TENG by finger tapping both keep almost the same at the 0th, 100th, 500th, and 1000th cycles, demonstrating the high flexibility and performance stability of the developed Cu-BHT films and devices.

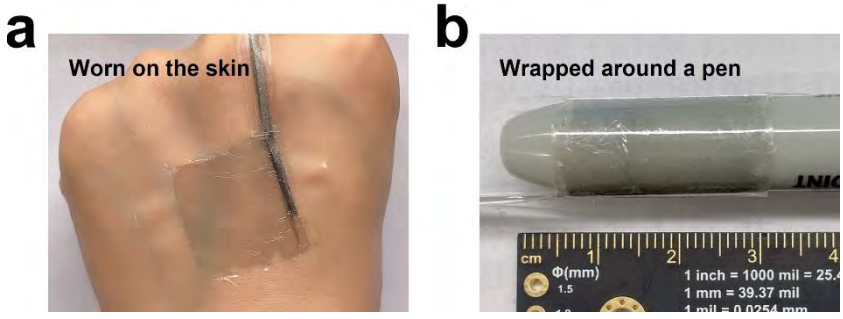

Fig. S16. PCL/Cu-BHT/PVC TENG was a) worn on human skin and b) wrapped around a pen with a

diameter of 1 cm.

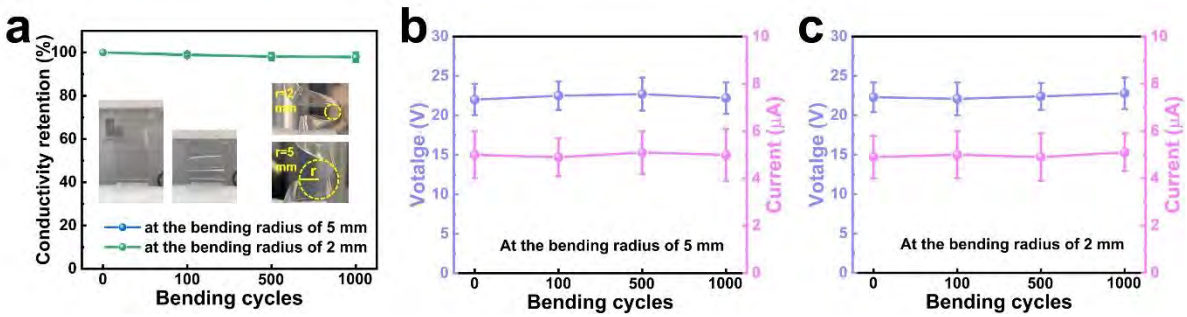

Fig. S17. a) Conductivity stability Cu-BHT/PCL films after bending at a radius of 5 mm for 0, 100, 500, 1000 cycles, and output stability of PCL/Cu-BHT/PVC TENG after bending at a radius of b) 5 mm and c) 2 mm for 0, 100, 500, 1000 cycles.

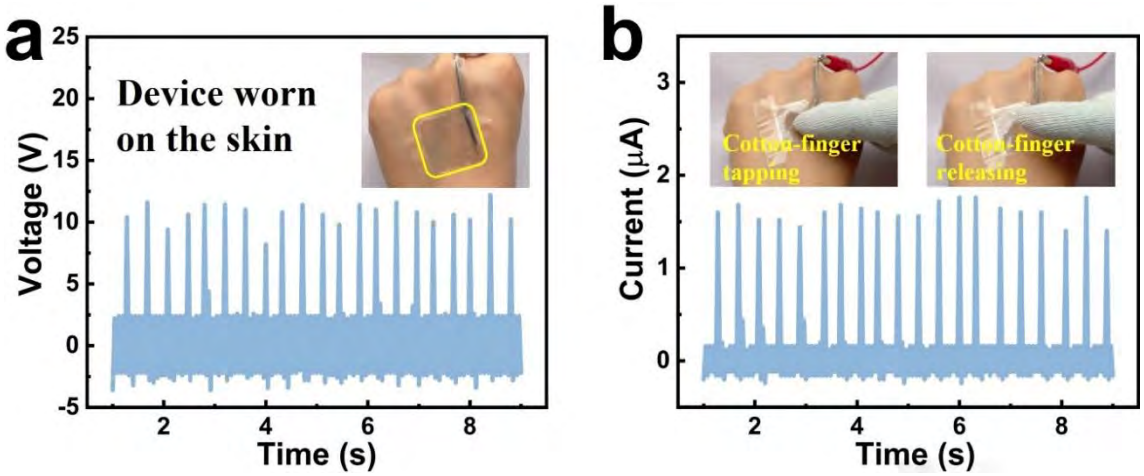

Fig. S18. Output a) voltage and b) current signals generated by the index finger worn a cotton glove tapping the device.

5. Device Performance Comparison

As shown in Table S1 and Table S2, the developed Cu-BHT TENG in this work shows excellent output performance in both droplet and human motion energy harvesting.

Table S1. Output performance comparison with common TENGs in droplet energy harvesting.

Ref.	Device structure	Droplet Type	Droplet volume	Voltage (V)	Current (μA)	Power (μW)
[S5]	Leaf blade /petiole	0.1M NaCl	33 μL	1.3	4.1 (rain 1μA)	1
[S6]	Ag/PDMS/Ag/Si /Al	Rainwater	20 μL	~38	~11	183

[S7]	HDL/ITO/PDMS/VHB	DI water Tap water	110 μL	~62 ~59	/	21.5 (215 mW/m^2)
[S8]	PTFE/Cu/Kapton	Rainwater	(22 mL/s)	28.9	9.1	/
[S9]	EVA/CF/MF/rubber	Rainwater	120 μL	~0.42	~0.03	/
[S10]	PTFE/Ag/Nylon	DI water/Rainwater Tap water/0.6M NaCl	40 μL	5.2/4.6 3.0/1.6	0.53/0.42 0.24/0.16	22.1/12.6 7.1/3.2
[S11]	Parylene/Ni	Rainwater/Tap water DI water	/	0.3/0.5 3.3	1.5/1.5 0.6	/
[S12]	PTFE/C-textile	DI water 0.015M/0.6M NaCl	50 μL	60 50/38	9 /	/
[S13]	Al/PTFE	Tap water 0.1M NaCl	100 μL	~60 ~30	/	/
[S14]	PTFE/C-fiber	Rainwater	/	~12	~0.8	/
This work	PCL/Cu-BHT/PVC	DI water/D water Tap water/rainwater	12.5 μL	21.7/25.3 29/28	2.35/6.7 78/41	15.6/71.8 337.5/216.8

(Note: here we only summarized droplet-TENGs that have provided the droplet type information, as the droplet type is one of the key factors that affects the output performance of droplet-TENG.)

Table S2. Output performance comparison with MOFs-TENGs in human motion energy harvesting.

Ref.	Device structure	Active area (cm^2)	Human motions	Voltage (V)	Current (μA)	Role of MOFs
[6]	Al/PDMS@F-MOF—Al	2×3	Hand tapping	~25	/	Tribo-negative material
[10]	Al/ZIF-62—Teflon/Al	2.5×2.5	Hands curls, shoulder press	5-8 V	/	Tribo-positive material
[11]	Al/Co-NPC-PVDF—Nylon	2.5×2.5	Walking slow running	100-150 V	/	Tribo-negative material
[13]	CA/Ni-HITP—PVDF	2.75×2.75 ×3.14	Normal/rapid breathing	1.3-1.5 V	/	Tribo-positive material
[S15]	Cu/Cyclodextrin—Teflon/Cu	2×2	Jogging	~40	~0.3	Tribo-positive material
[S16]	Al/MIL-88A—FEP/Al	2.5×2.5	Finger tapping	~18	/	Tribo-positive material
[S17]	Al/NF-MOF/SF—PDMS/Al	2×2.5	Clapping Stepping	~30-60	/	Tribo-positive material
This work	PCL/Cu-BHT/PVC	2×2	Finger tapping	22	5	electrode

6. References

[S1] G. Kresse, J. Furthmüller, *Phys. Rev. B* **54**, 11169 (1996).

[S2] P. E. Blöchl, *Phys. Rev. B* **50**, 17953 (1994).

[S3] J. P. Perdew, K. Burke, M. Ernzerhof, *Phys. Rev. Lett.* **77**, 3865-3868 (1996).

[S4] H. J. Monkhorst, J. D. Pack, *Phys. Rev. B* **13**, 5188-5192 (1976).

[S5] H. Wu, Z. Chen, G. Xu, J. Xu, Z. Wang, Y. Zi, ACS Appl. Mater. Interfaces **12**, 56060–56067 (2020).

[S6] L. Zhao, J. Duan, L. Liu, J. Wang, Y. Duan, L. Vaillant-Roca, X. Yang, Q. Tang, Nano Energy **82**, 105773 (2021).

[S7] J. Wang, L. Ma, J. He, Y. Yao, X. Zhu, L. Peng, J. Yang, K. Li, M. Qu, Chem. Eng. J. **431**, 134002 (2022).

[S8] X. Liu, A. Yu, A. Qin, J. Zhai, Adv. Mater. Technol. **4**, 1900608 (2019).

[S9] Y-C. Lai, Y-C. Hisao, H-M. Wu, Z. L. Wang, Adv. Sci. **6**, 1801883 (2019).

[S10] L. Zhao, L. Liu, X. Yang, H. Hong, Q. Yang, J. Wang, Q. Tang, J. Mater. Chem. A **8**, 7880–7888 (2020).

[S11] X. Gang, Z. H. Guo, Z. Cong, J. Wang, C. Chang, C. Pan, X. Pu, Z. L. Wang, ACS Appl. Mater. Interfaces **13**, 20145–20152 (2021).

[S12] F. Liang, X. Chao, S. Yu, Y. Gu, X. Zhang, X. Wei, J. Fan, X. Tao, D. Shou, Adv. Energy Mater. **12**, 2102991 (2022).

[S13] N. Zhang, H. Gu, K. Lu, S. Ye, W. Xu, H. Zheng, Y. Song, C. Liu, J. Jiao, Z. Wang, X. Zhou, Nano Energy **82**, 105735 (2021).

[S14] W. Yuan, C. Zhang, B. Zhang, X. Wei, O. Yang, Y. Liu, L. He, S. Cui, J. Wang, Z. L. Wang, Adv. Mater. Technol. 2101139 (2021).

[S15] S. Hajra, M. Sahu, A. M. Padhan, I. S. Lee, D. K. Yi, P. Alagarsamy, S. S. Nanda, H. J. Kim, Adv. Funct. Mater. **31**, 2101829 (2021).

[S16] G. Khandelwal, N. P. M. J. Raj, V. Vivekananthan, S.-J. Kim, iScience **24**, 102064 (2019).

[S17] Z. Chen, Y. Cao, W. Yang, L. An, H. Fan, Y. Guo, J. Mater. Chem. A **10**, 799–807 (2022).